Article

Laser Beam Self-Focusing in Silicon at an Absorbed Wavelength by a Vortex Beam in the Same Wavelength

Nadav Shabairou, Zeev Zalevsky, and Moshe Sinvani*

Cite This: *ACS Omega* 2024, 9, 16969−16975

Read Online

ACCESS | Metrics & More | Article Recommendations

ABSTRACT: In this research, we present a novel approach to achieving super-resolution in silicon using the plasma dispersion effect (PDE) that temporarily controls the complex refractive index of matter. By employing a laser vortex pump beam, which is absorbed in the silicon, we can shape the complex refractive index as a gradient index (GRIN) lens, enabling the focusing of a laser probe beam within the material. Our study introduces a single beam at a wavelength of 775 nm for both the pump and the probe beams, offering tunable focusing capabilities and the potential to attain higher spatial resolution. These findings hold significant promise for applications in nanoelectronics and integrated circuit failure analysis, paving the way for advanced semiconductor imaging and analysis techniques.
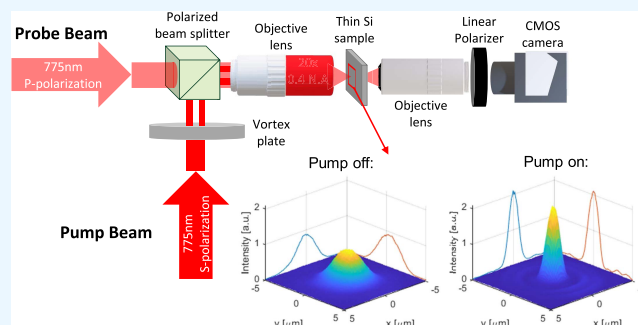
INTRODUCTION

Super-resolution imaging has revolutionized various scientific and technological fields by enabling the resolution of details beyond the diffraction limits of traditional optical systems. Overcoming diffraction limitations has been a long-standing challenge, and researchers have explored various strategies to enhance resolution.[1,2] In recent years, structured light, particularly vortex laser beams, has gained significant attention due to their unique properties and potential for surpassing the diffraction limit.[3−5]

Our research aims to achieve super-resolution in semiconductors by temporally and spatially controlling their complex index of refraction. Specifically, in silicon bulk samples, we have successfully demonstrated super-resolution and focusing of an infrared (IR) probe beam with a wavelength of 1550 nm and a pulse width of 50 ps.[6,7] Our approach involves introducing a second laser beam, acting as a pump beam, which is absorbed in the silicon and temporally induces a pattern of free charge carriers (FCCs) within the sample, corresponding to the size of the pump beam spot. The FCCs generate a change in the index of refraction according to the spatial intensity distribution of the pump beam, resulting in a reduced index of refraction and increased absorption within the FCCs pattern. According to the PDE and in proportion to its spatial intensity distribution, the index of refraction of the FCCs pattern is reduced, and the absorption is increased.[8] In our initial experiment,[6] we employed a Gaussian pump beam with a wavelength of 532 nm and a pulse width of 17 ns. The point spread function (PSF) of the pump beam we chose was narrower by a factor of 3 in comparison with the PSF of the

probe beam. Both beams were introduced on the sample collinearly and temporally, with the probe beam pulses slightly delayed compared to the pump beam pulses. The pump beam shapes the PSF by controlling the lateral transmission of the IR probe beam. The image of the transmitted wide probe beam shows a small block of the probe beam in its center, splitting the beam profile into two thinner PSF parts. We demonstrated super-resolution in silicon by scanning a 3-bar resolution target with the shaped probe beam. However, our attempt to achieve focusing by converting the pump beam into a donut shape using a vortex plate was unconvinced due to the diffusion time of the FCCs, which was incompatible with the relatively long pump pulse duration.

In follow-up research,[7] we utilized a new laser with a narrower pulse width of 30 ps and two harmonics, employing a wavelength of 1550 nm for the probe beam and 775 nm for the pump beam. This experimental setup yielded focusing with a point spread function (PSF) of ∼2 μm. The vortex pump beam induced a ring of decreased refractive index value within the material, gradually increasing toward the natural refractive index of the silicon in its periphery. The outer region of the donut caused defocusing, while the inner part acted as a
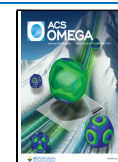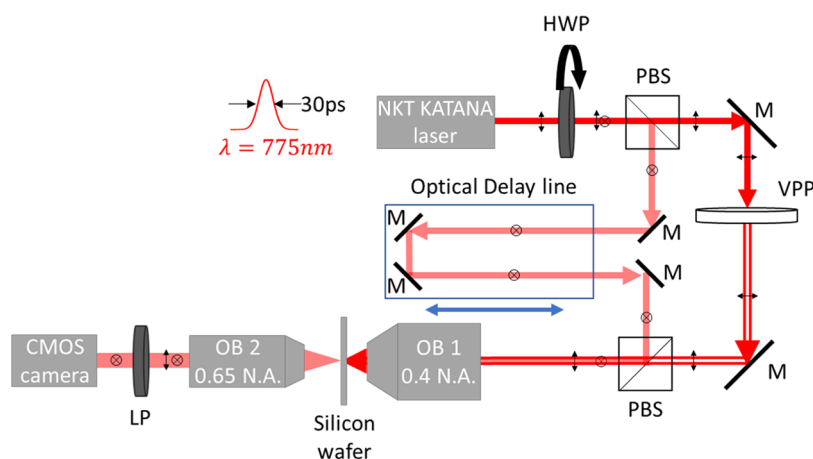
Figure 1. Experimental setup. Abbreviation: HWP, half-waveplate; LP, linear polarizer; M, mirror; PBS, polarization beam splitter cube; OB, objective lens; P and S polarizations represented on and perpendicular to the page arrows, respectively.
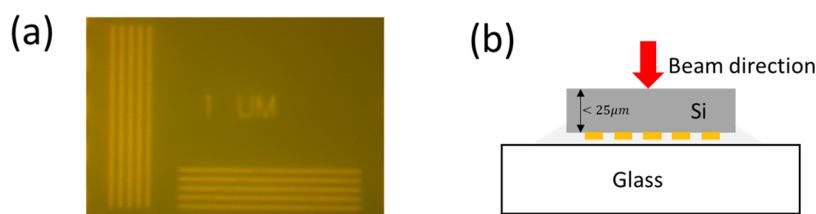

Figure 2. Sample: microscopic image of the gold stripe resolution target on the silicon surface (a) and cross-section illustration of the sample at the resolution target (b).

gradient index (GRIN) lens, effectively focusing the probe beam toward the center of the ring. Notably, using a pump beam of 775 nm allowed deeper focusing inside the sample due to the absorption depth of ~8 μm in silicon for this wavelength.[9,10] However, we must thin the sample to ~20 μm to allow some transmission of the probe beam.

In the present work, we use a probe beam with the same wavelength of 775 nm as for the pump beam instead of the 1550 nm we used before. We separated a laser beam at a wavelength of 775 nm into two beams with orthogonal polarizations to distinguish between them. One beam converts to a vortex shape and serves as a pump beam; the other stays in a Gaussian shape and is the probe beam. This configuration enabled us to observe the focusing of a probe beam with photon energy above the band gap energy to gain spatial resolution by decreasing the probe wavelength. It also enabled us to observe the focusing of a probe beam resulting from variations in the pump beam intensity, even at shorter wavelengths, while also facilitating the study of the self-focusing effect induced by the optical vortex pump beam.

Furthermore, this approach offers the potential to achieve higher resolution by a factor of 2 compared to our previous work due to the reduced wavelength of the probe beam by a factor of 2. By adjusting the pulse intensity that governs the spatial shape of the beam, we can control the focusing degree. Such tunable focusing capabilities hold significant promise for surpassing the diffraction resolution limit in silicon microscopy, offering valuable applications in nanoelectronics, particularly in integrated circuit (IC) failure analysis and 3D writing in silicon. Moreover, using the same laser for the two beams can be very important for the engineering of the design of silicon microscopy.

METHODS

Experimental Setup. The experimental setup is depicted in Figure 1. We used a picosecond laser (NKT Onefive KATANA 8) with a wavelength of 775 nm and a pulse width of 30 ps. The laser beam was divided into pump and probe beams by using a half-waveplate (HWP, Thorlabs) and a polarization beam splitter cube (PBS 1, Thorlabs), which split the beam into two orthogonal polarization beams (S and P). The P polarization (the arrows in the plane of the page) was set as the pump beam, and the S polarization (the arrows perpendicular to the page) was set as the probe beam. The rotation of the HWP manipulated the intensity ratio between the two beams. We usually set it to a pump−probe ratio of 100:1, respectively. The phase plate (RPC PHOTONICS VPP-m780) shaped the pump beam into a vortex beam with a topological charge of order 1. The probe beam was passed through an optical delay line to adjust the pump−probe delay time. We adjusted the delay time to 60 ps to prevent overlap between the pump and probe beams and to approve the arrival of the probe pulse just after the pump beam and the complete generation of the FCCs. The pump and probe beams were combined with PBS 2 and focused by an objective lens with a numerical aperture (N.A.) of 0.40 on the silicon sample. The transmitted light was collected by an objective (OB 2) with an N.A. of 0.65 and imaged on a CMOS camera sensor. A linear polarizer (LP) was introduced between the objective lens and camera to allow capture of either the probe or the pump beam.

Sample Preparation. To demonstrate the resolution improvement, we fabricated a resolution target on the rear side of the silicon sample. The resolution target consists of five gold stripes, each with a width of 1 μm and evenly spaced 1 μm between them. The target was glued on a microscope slide by wax adhesive (Crystalbond 509-3), where the gold stripes
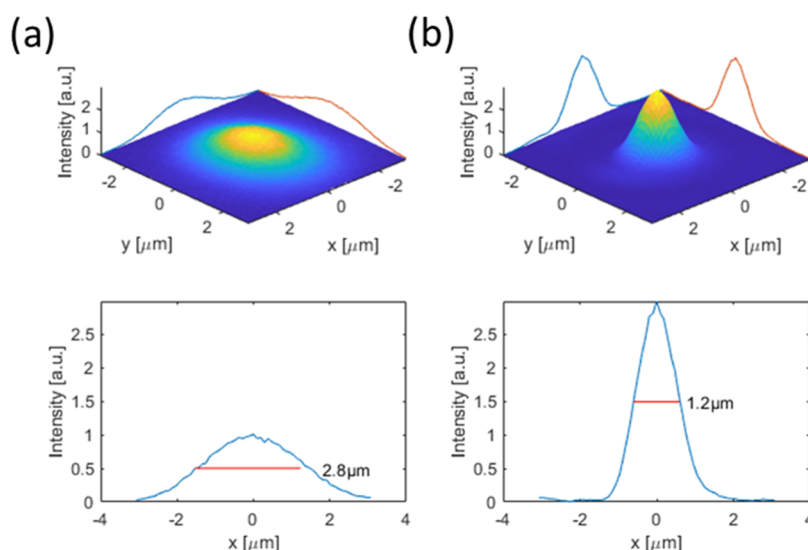
Figure 3. Focusing phenomenon experimental. The image of the transmitted probe beam when the pump is off ($E = 0$ nJ) (a) and with a pulse pump energy of 35 nJ (b) was applied to show the focusing.

faced toward the glass, as shown in Figure 2. The silicon sample was polished to a thickness of 25 μm, which is where the probe beam is focused approximately. The target was mounted on a linear x−y−z piezo-stage (PI P-611.3 Nano Cube), enabling precise nanometric movements during scanning operations.

RESULTS AND DISCUSSION

The image of the transmitted probe beam through the sample is shown in Figure 3 for the two states. First, when the pump beam is off (Figure 3a) and second, when it is shaped by the pump beam with a pulse energy of 35 nJ (Figure 3b). The full width at half-maximum (fwhm) of the probe beam was reduced from 2.8 to 1.2 μm when the pump beam was applied. The peak intensity of the shaped beam increased, but the total intensity of the transmitted beam was reduced. This behavior occurs due to the increased absorption coefficient in higher FCCs concentration, which decreases the overall transmitted intensity.

To examine the propagation of the probe beam inside the temporally modified material due to the pump beam pulse, we conducted numerical simulations to enhance our model for studying the focusing parameters. The simulation was designed in two main stages. The initial stage aimed to determine the spatial pattern of the complex refractive index induced in the semiconductor by a pump beam. To model the intensity distribution of the pump beam, we utilized the analytic equation of the Laguerre−Gaussian beam in cylindrical coordinates[11]

$$
E_{l,m}(r, \phi, z) = \frac{E_0}{\sqrt{1 + z^2/z_R^2}} \left(\frac{r\sqrt{2}}{w(z)} \right)^{|l|}
$$

$$
\cdot L_p^{|l|} \left(\frac{2r^2}{w^2(z)} \right) \cdot \exp\left(-\frac{r^2}{w^2(z)} \right) \cdot
$$

$$
\exp\left(-ikz - \frac{ikr^2z}{2(z_R^2 + z^2)} - il\phi \right.
$$

$$
\left. + i(2p + l + 1)\arctan\left(\frac{z}{z_R} \right) \right) \tag{1}
$$

where z_R is the Rayleigh range, $w(z)$ is the radius of the beam, $L_p^{|l|}$ is the associated Laguerre polynomial, l is the azimuthal mode index, p is the radial index, E_0 is a constant, and w_0 the beam waist is at $z = 0$. The radius of the beam $w(z)$ is defined by

$$
w(z) = w_0 \sqrt{1 + \frac{z^2}{z_R^2}} \tag{2}
$$

The distribution of the pattern of the pump photons, which are absorbed inside the semiconductor, was calculated according to the intensity loss along the light propagation axis in the silicon (Beer−Lambert law). We assumed a quantum efficiency of one, where each pump photon generates a single electron−hole pair. The FCCs distribution pattern is translated to a change in the dielectric constant in the silicon and can be described by the Drude model[12]

$$
\Delta\varepsilon_{fcc} = -\frac{e^2}{\varepsilon_0 m_e \omega^2} \left(\frac{N_e}{m_e^*} + \frac{N_h}{m_h^*} \right) \left(\frac{1}{1 + i/\omega\tau_D} \right) \tag{3}
$$

where ε_0, m_e, ω, m_e^*, and m_h^* are the vacuum permittivity, electron mass, excitation frequency, and mobility-effective mass of electrons and holes, respectively. For the Drude damping time τ_D, we chose a value of $\tau_D = 10^{-14}$ [s], which corresponded to high FCCs concentration[13] (above 10^{19} cm^{-3}). The simulation was done on the 2-dimensional cross section of the XZ plane along the center of the beam, assuming
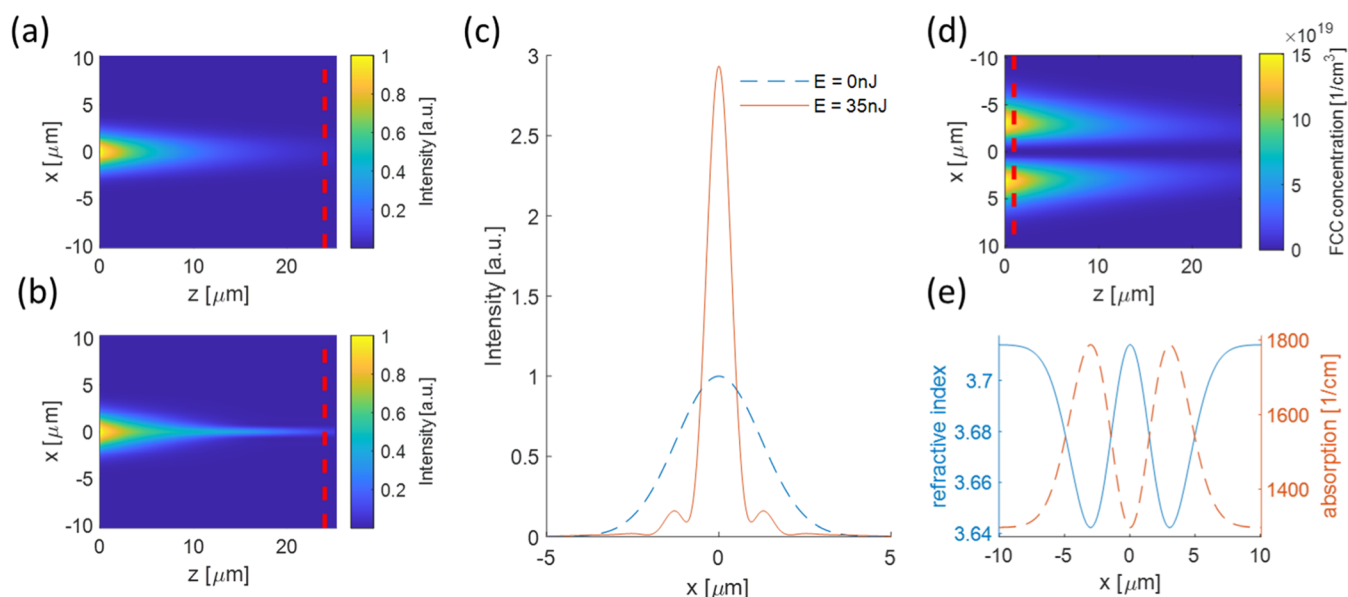
Figure 4. Numerical calculation results for a GRIN lens induced in silicon by an optical vortex pump beam. The propagation of the probe beam alone in the sample along the z-axis is shown in panel (a) and with the pump beam in panel (b). The beam profiles along the red dash lines in panels (a) and (b) are illustrated in panel (c), demonstrating the focusing of the probe beam due to the pump beam application (red peak). The FCCs concentration, excited by the pump beam, is shown in panel (d). The refractive index and the corresponding absorption coefficient along the red dashed line in panel (d) are shown in panel (e).
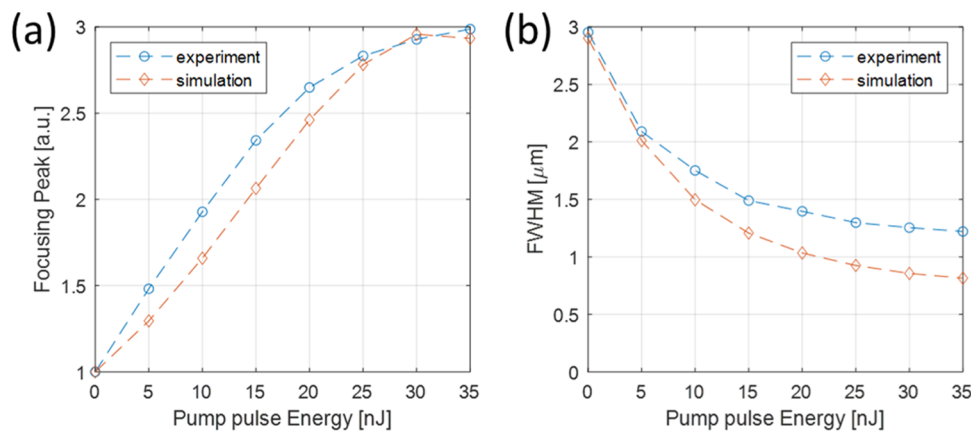

Figure 5. Focusing peak intensity (a) and focusing fwhm (b) as a function of the pump pulse energy.

radial symmetry in the XY plane. In the last step, we simulated the propagation of the probe beam according to the temporal distribution of the FCCs in the silicon. The simulation was performed by using the finite-difference frequency-domain (FDFD) method.[14]

In Figure 4, simulation results are presented to demonstrate the focusing effect of a 775 nm Gaussian probe beam by a 775 nm vortex pump beam in two states: first, without the pump beam (Figure 4a) and second, with the pump beam at a pulse energy of 35 nJ (Figure 4b). The donut-shaped pump beam, with a diameter of 6 μm, is colinear with the probe beam, and its profile is shown along the z-axis, representing the propagation direction of the beams. Figure 4c displays the shape of the probe beam at 24 μm inside the sample, demonstrating focusing under the pump beam application. Additionally, Figure 4d shows a cross section of the free charge carriers (FCCs) pattern excited by the pump beam along the propagation axis z. A profile of the calculated refractive index and the corresponding absorption coefficient, along the red

dashed line in Figure 4d, is shown in Figure 4e. The increase in FCCs concentration results in a decrease in the refractive index and an increase in the absorption coefficient following the PDE. Consequently, the pump beam creates a ring pattern of a reduced index of refraction in its diameter in the silicon that increases gradually to the standard value of the matter. The gradual increase in the distribution of the index of refraction from the ring contour inside to its center effectively creates a sort of gradient index-like (GRIN) lens. As a result, the light passing through the inner region of the FCCs donut pattern becomes focused, exhibiting lens-like behavior. For FCCs, concentration around 10^{20} cm^{-3}, we get a change in the real part of the refractive index of ~0.05 at 775 nm compared to ~0.2 at the wavelength of 1550 nm, which is four times higher as the change goes as λ^2, according to the Drude model. Nevertheless, it can be seen in the simulation and in the experiment that the refractive index change is sufficient to induce focus inside the material. The lens is created inside the material; therefore, the diffraction limit decreases by the factor
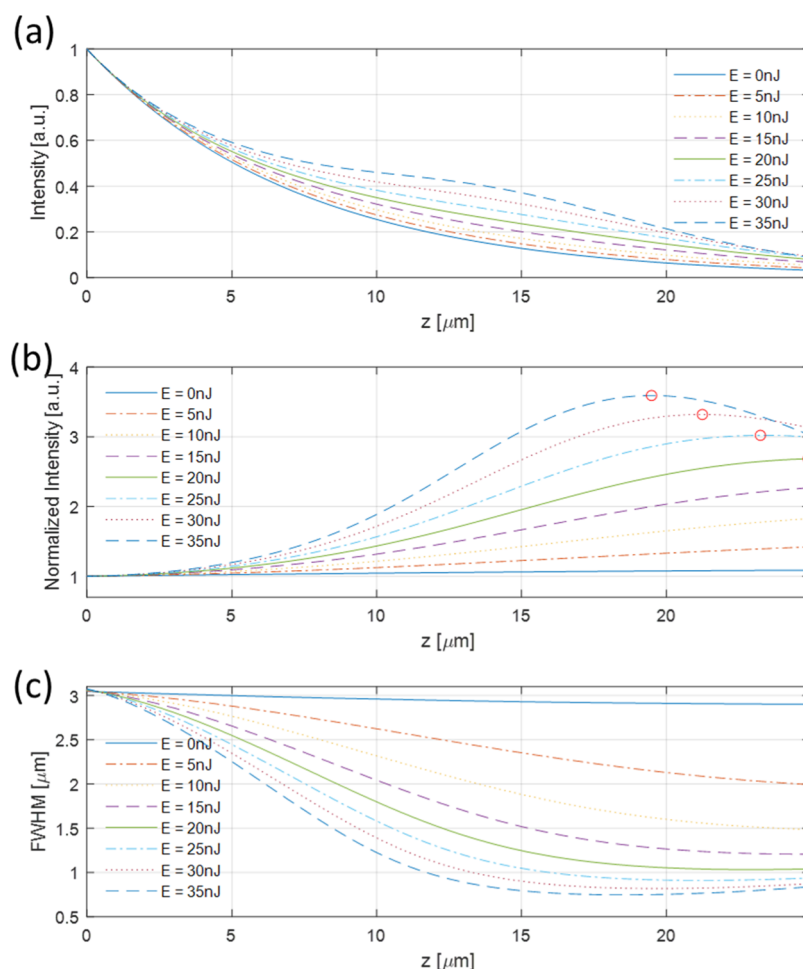
Figure 6. Focus by simulation. In panel (a), given the results for the on-axis intensity of the probe beam inside the silicon for different pump pulse energy E and in panel (b), after normalizing the pump intensity according to Beer−Lambert law absorption at 775 nm. The red circles mark the peak intensity and indicate the focus location at each pump intensity. At $E = 20$ nJ, the probe focused at $z = 25$ μm. In panel (c) is given the width of the probe beam along the z-axis for various pump intensities. We must emphasize that at $E = 0$ nJ, the probe beam focused on the sample's back surface (at $z = 25$ μm).

of the refractive index, allowing it to overcome the diffraction limit of the illuminating objective lens (OB1).

The GRIN lens focal width is determined by the slope (dn/dx) of its lateral gradient index (see Figure 4e). Therefore, by increasing the intensity of the pump beam, we can enhance the gradient index slope, allowing for manipulation of the focus parameters by adjusting the concentration of the (FCCs). Figure 5 shows the relationship between the pump pulse energy and the peak intensity with its width at the rear surface of the sample, in both simulation and experiment. The width of the focused probe beam (Figure 5b) decreases as the pump intensity increases, indicating an improvement in the focusing. Furthermore, the peak intensity (Figure 5a) exhibits a linear increase at lower pump pulse energies. In comparison, a saturation-like behavior of the peak intensity is observed at higher energies, which will be discussed later.

Figure 6a illustrates the on-axis intensity of the probe beam at varying pump intensities. In lossless materials, the peak intensity would align with the focus along the propagation direction (z-axis). However, the material's absorption causes a shift in the peak intensity, positioned away from the focal point. To account for this absorption, we normalize the intensity along the z-axis (Figure 6b) using the term $e^{-\alpha z}$ (Beer−Lambert law), where α denotes the silicon absorption

coefficient at a wavelength of 775 nm. The focal distance decreases as the pump intensity increases, eventually causing the focus to move into the sample. This observation can explain the saturation-like behavior of the peak intensity we observe in Figure 5a. We can also see that as the intensity of the pump beam increases, the width of the beam decreases, and at a certain point ($E > 20$ nJ), the minimum width is inside the material. Consequently, as the focus shifts from the rear surface to the material, the peak intensity decreases, and the width expands, indicating a loss of focus. Figure 6c shows the fwhm of the probe beam along the z-axis for various values of pump energies E. We can see that the probe beam at $E = 0$ nJ, without a pump beam, the focus is very shallow across the sample. In the simulation, we introduced the probe beam on the sample with NA = 0.1 and set it to be focused on the rear surface of the sample at $z = 25$ μm. When we applied the pump beam, we dramatically reduced the spot size by a factor of ~3 and extended the focus depth.

To illustrate the resolution enhancement by sharpening the probe beam with a vortex pump beam, we conducted a scan across the resolution target. As mentioned above, the target comprises a 5-bar gold grating on the rear surface of the silicon sample (see Figure 2b). The probe was focused on the resolution target. The silicon sample was shifted at 50 nm step
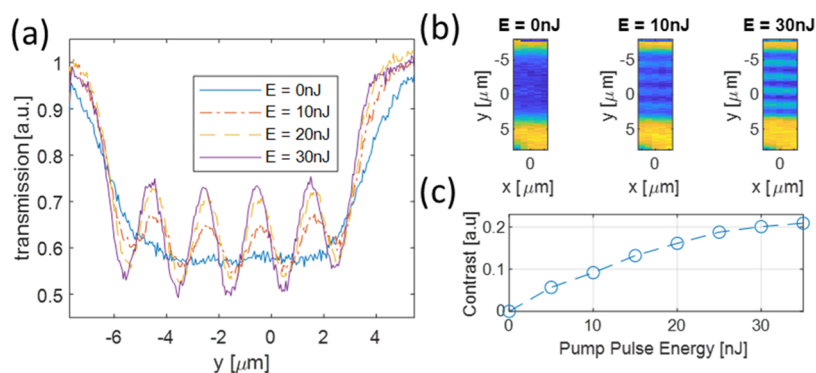
Figure 7. Super-resolution imaging of the resolution target using a shaped probe beam modulated by a pump beam at varying intensities. (a) Cross section along a resolution target. (b) Reconstructed images of the resolution target at different pump intensities. (c) Calculated contrast as a function of the pump pulse energy.
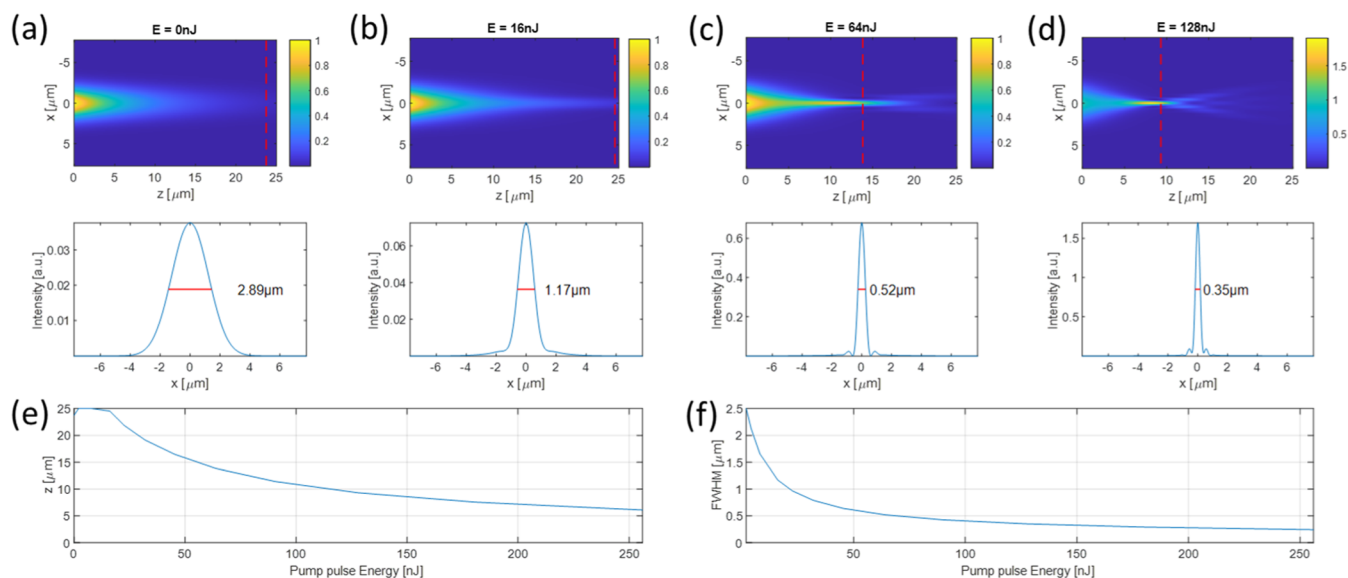

Figure 8. Simulation results illustrate the propagation of the probe beam under high pump intensities. The images demonstrate the probe beam's propagation along the z-axis and its intensity profile at the focal point for varying pump pulse energies: (a) $E = 0$ nJ, (b) $E = 16$ nJ, (c) $E = 64$ nJ, and (d) $E = 128$ nJ. The focus location of the probe beam (e) and focus width (f) as a function of the pump pulse energy E.

size to scan the resolution target. At each step, the total transmitted intensity of the probe was measured by summing all of the camera's pixels. The scanning process was repeated for different pump pulse energies. In the result visualized in Figure 7, without the pump ($E = 0$ nJ), the width (fwhm) of the PSF was approximately 2.8 μm, which was insufficient to resolve the details of the resolution target. As the pump energy increased, we started to observe the bars of the resolution target, as shown in (a, b). The results show a significantly reduced PSF size and resolution improvement obtained with increasing pulse energies. To quantitatively assess the resolution improvement, we calculated the contrast using the standard contrast calculation method for gratings (Figure 7c)

$$\text{contrast} = \frac{I_{\max} - I_{\min}}{I_{\max} + I_{\min}} \tag{4}$$

where $I_{\max}$ is the transmission of the probe beam between two target bars and $I_{\min}$ is the transmission on a target bar. The contrast behavior observed in our experiment followed a trend similar to the peak intensity (see Figure 5a).

Figure 8 presents the simulation results of focusing the probe beam under a higher pump intensity application. The parameters in this simulation in continue to Figure 5. As we increase the intensity of the pump beam, both the width and the focal length decrease. Notably, the PSF created is significantly smaller, almost an order of magnitude, than the PSF when the pump beam is not applied.

Abbe's law defines the diffraction limit of a system as $\lambda/2\text{NA}$. For pulse energy $E = 128$ nJ (Figure 8d), the spot size is smaller than the maximum diffraction limit that can theoretically be created in the air at NA = 1. It is because the lens was induced inside the material, and therefore, its diffraction limit is smaller by the factor of the material's refractive index.

While methods such as the solid immersion lens (SIL)[15] fill the space between the lens and the surface with silicon to reach the diffraction limit of the material, these require direct contact with the surface. In contrast, our method shapes the beam inside the material using an objective lens with a low NA. Therefore, it enables us to achieve high resolution within the material without surface contact.

The depth of the focusing can be increased using a pump with longer wavelengths. This allows for the production of the lens deeper inside the silicon, enabling us to focus in the depth

of the silicon as opposed to short wavelengths, where most of the energy is concentrated near the surface. The choice of the pump wavelength will depend on the application.

However, one significant limitation is the power of the pump beam. When we reach a free carrier concentration of approximately $\sim10^{21}$ cm^{-3},[13,16] it can damage the silicon and affect the maximum focus that can be achieved.

CONCLUSIONS

We demonstrated super-resolution imaging in silicon by manipulating its complex refractive index using pump and probe beams at the same wavelength of 775 nm. Numerical simulations confirmed the temporary formation of a GRIN lens within the silicon that focuses the probe beam in the semiconducting medium. Also, using the same wavelength for both the pump and probe beams benefits the engineering of this kind of microscope. At the same time, this feature is in addition to the factor 2 improvement in the resolution.

Experimental and numerical simulation results showed that the pump beam significantly affected the transmitted probe beam, leading to its focus inside the silicon. The findings have important implications for high-resolution imaging in challenging environments, opening new possibilities for applications in various fields, including nanoelectronics and the failure analysis of integrated circuits.

ASSOCIATED CONTENT

Data Availability Statement
The data underlying this study is provided within the manuscript. The raw data is available from the corresponding author upon reasonable request.

AUTHOR INFORMATION

Corresponding Author
> **Moshe Sinvani** − *Faculty of Engineering and the Nano-Technology Center, Bar-Ilan University, Ramat Gan 52900, Israel;* ⊙ orcid.org/0000-0001-9271-0242;
> Email: sinvanm@gmail.com

Authors
> **Nadav Shabairou** − *Faculty of Engineering and the Nano-Technology Center, Bar-Ilan University, Ramat Gan 52900, Israel*
> **Zeev Zalevsky** − *Faculty of Engineering and the Nano-Technology Center, Bar-Ilan University, Ramat Gan 52900, Israel;* ⊙ orcid.org/0000-0002-4459-3421

Complete contact information is available at:
https://pubs.acs.org/10.1021/acsomega.3c08325

Notes
The authors declare no competing financial interest.

ACKNOWLEDGMENTS

ABBREVIATIONS

PDE –plasma dispersion effect
PSF –point spread function
fwhm –full width at half-maximum
FCC –free charge carrier
GRIN –gradient index

REFERENCES

(1) Huszka, G.; Gijs, M. A. M. Super-Resolution Optical Imaging: A Comparison. *Micro Nano Eng.* **2019**, *2*, 7−28.
(2) Zalevsky, Z.; Mendlovic, D. *Optical Superresolution*; Springer Science & Business Media, 2004.
(3) Shen, Y.; Wang, X.; Xie, Z.; Min, C.; Fu, X.; Liu, Q.; Gong, M.; Yuan, X. Optical Vortices 30 Years on: OAM Manipulation from Topological Charge to Multiple Singularities. *Light: Sci. Appl.* **2019**, *8* (1), 90.
(4) Tamburini, F.; Anzolin, G.; Umbriaco, G.; Bianchini, A.; Barbieri, C. Overcoming the Rayleigh Criterion Limit with Optical Vortices. *Phys. Rev. Lett.* **2006**, *97* (16), No. 163903.
(5) Willig, K. I.; Rizzoli, S. O.; Westphal, V.; Jahn, R.; Hell, S. W. STED Microscopy Reveals That Synaptotagmin Remains Clustered after Synaptic Vesicle Exocytosis. *Nature* **2006**, *440* (7086), 935−939.
(6) Pinhas, H.; Wagner, O.; Danan, Y.; Danino, M.; Zalevsky, Z.; Sinvani, M. Plasma Dispersion Effect Based Super-Resolved Imaging in Silicon. *Opt. Express* **2018**, *26* (19), 25370−25380.
(7) Shabairou, N.; Tiferet, M.; Zalevsky, Z.; Sinvani, M. Dynamics of Laser-Induced Tunable Focusing in Silicon. *Sci. Rep.* **2022**, *12* (1), No. 6342.
(8) Soref, R.; Bennett, B. Electrooptical Effects in Silicon. *IEEE J. Quantum Electron.* **1987**, *23* (1), 123−129.
(9) Johnson, P. B.; Christy, R. W. Optical Constants of the Noble Metals. *Phys. Rev. B* **1972**, *6* (12), 4370−4379.
(10) Palik, E. D. *Handbook of Optical Constants of Solids*; Academic Press, 1998.
(11) Allen, L.; Beijersbergen, M. W.; Spreeuw, R. J. C.; Woerdman, J. P. Orbital Angular Momentum of Light and the Transformation of Laguerre-Gaussian Laser Modes. *Phys. Rev. A* **1992**, *45* (11), 8185−8189.
(12) Ziman, J. M. *Principles of the Theory of Solids*; Cambridge University Press, 1972.
(13) Sokolowski-Tinten, K.; von der Linde, D. Generation of Dense Electron-Hole Plasmas in Silicon. *Phys. Rev. B* **2000**, *61* (4), 2643−2650.
(14) Shin, W.; Fan, S. Choice of the Perfectly Matched Layer Boundary Condition for Frequency-Domain Maxwell's Equations Solvers. *J. Comput. Phys.* **2012**, *231* (8), 3406−3431.
(15) Ramsay, E. Solid Immersion Lens Applications for Nanophotonic Devices. *J. Nanophoton* **2008**, *2* (1), No. 021854.
(16) Mouskeftaras, A.; Rode, A. V.; Clady, R.; Sentis, M.; Utéza, O.; Grojo, D. Self-Limited Underdense Microplasmas in Bulk Silicon Induced by Ultrashort Laser Pulses. *Appl. Phys. Lett.* **2014**, *105* (19), No. 191103.